INTERNATIONAL JOURNAL FOR NUMERICAL METHODS IN FLUIDS, VOL. 14, 1087–1109 (1992)

CALCULATION OF TWO-DIMENSIONAL SHEAR-DRIVEN CAVITY FLOWS AT HIGH REYNOLDS NUMBERS

A. HUSER AND S. BIRINGEN

Department of Aerospace Engineering Sciences, University of Colorado, Boulder, CO 80309, U.S.A.

SUMMARY

The time-dependent Navier–Stokes equations are numerically integrated for two-dimensional incompressible viscous flow in a shear-driven square cavity. Using a time-splitting method and finite differences on a staggered mesh, the momentum and pressure equations are directly solved by a tensor product method where one finite difference direction is diagonalized by eigenvalue decomposition. The effects of increasing Reynolds number are studied and the developing boundary layer is captured by using a finely clustered mesh. At $Re = 30\,000$ the flow is in a continuously developing unsteady regime. Power spectrum plots indicate that the unsteady flow oscillates with one fundamental frequency and exhibits some characteristics of transition between laminar and turbulent states.

KEY WORDS Unsteady cavity flows

1. INTRODUCTION

Cavity flows have been frequently employed to test the accuracy of Navier–Stokes solvers, with the isothermal, square, lid-driven cavity being the most popular. A comprehensive survey of numerical work on lid-driven flows is given by Ghia *et al.*,[1] who studied the vortex dynamics at high Reynolds numbers. Recently Biringen and Danabasoglu[2] investigated a cavity flow with an oscillating lid and with surface heating. The shear-driven cavity flow is closely related to the lid-driven flow, the only difference being the definition of the driving force, which is a constant surface velocity gradient in the former (free surface with no deformation) and a constant surface velocity in the latter (solid boundary). In this work, by addressing the shear-driven cavity flow rather than the well investigated lid-driven cavity flow, we will display some novel results, even though the basic physics of the two flows is similar. Of the few numerical simulations concerning shear-driven cavity flows, Kumagai's[3] work addresses the effects of aspect ratio at moderate Reynolds numbers and provides comparisons with the earlier work of Bye.[4] The shear-driven cavity flow is also of interest becuase of its similarity to wind-driven flows and can be useful to assess the momentum transport from air to water when the effect of waves on the interface is neglected. In an experimental study Wu[5] investigated the effects of waves in a shallow, long tank and deduced that the momentum transport from air to water due to wave motion on the interface is important for the Reynolds number range he considered. Wu[5] also found that when the effects of waves are taken into account, the surface current velocity is proportional to the wind friction velocity, a fact that is not valid for the present pure shear-driven flow. In the cases studied here, using lower Reynolds numbers than used by Wu[5] (about one order of magnitude lower) and the assumption that the interface is flat, a central question is to determine the onset of unsteady flow

0271–2091/92/091087–23$11.50

Received 26 February 1991
Revised 26 September 1991

as the Reynolds number increases. The unsteady time-asymptotic dynamics of two-dimensional recirculating flows has only recently received attention with increased computational capabilities[6] and is an informative way to investigate the behaviour of the non-linearities in the Navier–Stokes equations.

The purpose of this paper is to investigate two-dimensional shear-driven cavity flows at high Reynolds numbers with emphasis on the unsteady (unstable) state. Note that at this stage, before the flow becomes turbulent, the flow dynamics can be simulated only by a time-accurate computational model, which is the approach used in the present work. Kumagai's[3] work is based on the steady state vorticity equation, which cannot provide solutions in the unsteady flow regime at high Reynolds numbers. Consequently, in his work the flow behaviour at transition was inferred from the calculated velocity gradients in steady flow as the Reynolds number was increased.[3] In the present work we consider the time-dependent Navier–Stokes equations and use a time-accurate solution procedure capturing the true unsteadiness of the flow. Furthermore, since the present calculations were continued for very long integration times, the results are free from any long-term pseudotransients which may persist in cavity flow solutions at high Reynolds numbers.

Since the present computations are based on the two-dimensional Navier–Stokes equations, the influence of side walls is assumed to be negligible. We stress the fact that the main purpose of the paper is to demonstrate the differences between steady and unsteady numerical models in predicting the onset of oscillatory flow in two-dimensional cavities. At high Reynolds numbers three-dimensional effects due to end walls and spanwise aspect ratio become important,[7,8] but these effects are not considered here. However, on the basis of the two-dimensional computations of Sethian and Ghoniem[9] using the vortex method to calculate the two-dimensional turbulent flow over a backward-facing step, it can be asserted that time-dependent two-dimensional models can provide insight into the vortex dynamics in the unsteady flow regime. In this work, using a totally different solution technique for the same set of equations, we were also able to simulate the unsteadiness of high-Reynolds-number flows in shear-driven cavities and obtained an estimate for the Reynolds number at which the flow becomes oscillatory in the absence of side wall effects.

2. PROBLEM DEFINITION

We consider a two-dimensional square cavity containing water which is in contact with a steady air flow blowing over its surface (Figure 1). We assume that the boundary layer developed at the surface has a constant skin friction and that this friction drives the flow in the cavity. Consequently, at the air-water interface the shear stress $\tau = \rho_a u_*^2$ is constant; here u_* is the friction velocity at the interface. The governing equations are non-dimensionalized by the friction velocity u_* and the cavity height l. The governing equations that describe this incompressible, constant density flow are the continuity and Navier–Stokes equations, which can be written as

$$\frac{\partial \mathbf{u}}{\partial t} + \mathbf{u} \cdot \nabla \mathbf{u} = -\nabla p + \frac{1}{Re} \nabla^2 \mathbf{u}, \tag{1}$$

$$\nabla \cdot \mathbf{u} = 0. \tag{2}$$

Here the Renolds number is defined as $Re = lu_*/\nu$ and the physical constants used in the problem are the kinematic viscosity of water, $\nu = 10^{-6}\,\mathrm{m^2\,s^{-1}}$, the density of water, $\rho = 1000\,\mathrm{kg\,m^{-3}}$, and the density of air, $\rho_a = 1\,\mathrm{kg\,m^{-3}}$. These equations are solved with the following boundary conditions:

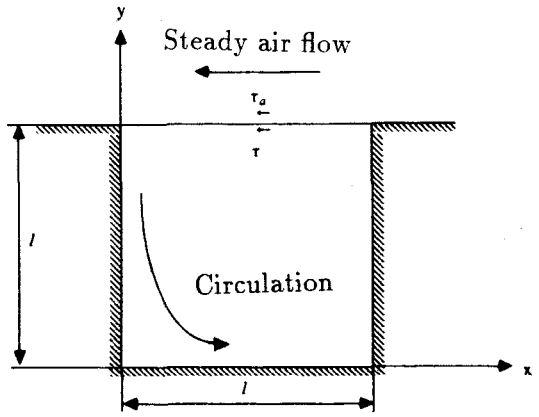

Figure 1. Flow geometry and co-ordinate system for shear-driven cavity

at the air–water interface,

$$\frac{\partial u}{\partial y} = -\frac{\rho_a}{\rho} Re \quad \text{and} \quad v = 0;$$

at the solid walls,

$$u = v = 0.$$

Note that there is no need for an explicit boundary condition for the pressure when using the time-splitting method explained in Section 3. In fact, it has been proven that homogeneous Neumann boundary conditions for the pressure ensure a consistent scheme *independent* of the Reynolds number at all types of boundaries, including solid walls and inflow/outflow boundaries.[10]

3. THE COMPUTATIONAL PROCEDURE

The Navier–Stokes equations describing this flow were solved by a modified version of the time-splitting method proposed by Kim and Moin.[11] In this section we briefly summarize the main points and expand on the techniques that were employed for the solution of the Helmholtz and Poisson equations obtained as a result of the time/space discretization. The time-splitting method involves two steps. During the intermediate step from t^n to $\hat{t}$ the following equation is solved:

$$\frac{\hat{\mathbf{u}} - \mathbf{u}^n}{\Delta t} = -\tfrac{3}{2}\mathbf{L}^n + \tfrac{1}{2}\mathbf{L}^{n-1} + \frac{1}{2Re}(\nabla^2 \hat{\mathbf{u}} + \nabla^2 \mathbf{u}^n) - \nabla p^n, \tag{3}$$

where $\mathbf{L} = \nabla \cdot (\mathbf{uu})$ and p is the computational pressure; also, temporal discretization is done with the Crank–Nicolson scheme on the viscous terms and the Adams–Bashforth method on the convective terms. Accordingly, the procedure is second-order-accurate in both time and space. For the time step from $\hat{t}$ to t^{n+1} we solve the equation

$$\frac{\mathbf{u}^{n+1} - \hat{\mathbf{u}}}{\Delta t} = -\tfrac{1}{2}(\nabla p^{n+1} - \nabla p^n). \tag{4}$$

Taking the divergence of (4) and considering that $\nabla \cdot \mathbf{u}^{n+1}$ vanishes because of continuity, the following equation has to be satisfied:

$$\frac{\nabla \cdot \hat{\mathbf{u}}}{\Delta t} = \tfrac{1}{2}(\nabla^2 p^{n+1} - \nabla^2 p^n). \tag{5}$$

After rearranging (3) and (5), the solution algorithm for each time step can be written as follows.

1. Solve for the $\hat{u}$- and $\hat{v}$-velocities using (3):

$$\frac{\hat{\mathbf{u}}}{\Delta t} - \frac{1}{2Re}\nabla^2 \hat{\mathbf{u}} = -\tfrac{3}{2}\mathbf{L}^n + \tfrac{1}{2}\mathbf{L}^{n-1} + \frac{1}{2Re}\nabla^2 \mathbf{u}^n + \frac{\mathbf{u}^n}{\Delta t} - \nabla p^n, \tag{6}$$

   with $\hat{\mathbf{u}} = 0$ at the walls and $\partial \hat{u}/\partial y = -(\rho_a/\rho)Re$ and $v = 0$ at the interface.
2. Solve for the pressure p^{n+1}:

$$\nabla^2 p^{n+1} = \frac{2}{\Delta t}\nabla \cdot \hat{\mathbf{u}} + \nabla^2 p^n, \tag{7}$$

   with $\partial p^{n+1}/\partial \mathbf{n} = 0$ at all four boundaries, where $\mathbf{n}$ is a vector normal to the boundary. This boundary condition follows from (4) with $\mathbf{u}^{n+1} = \hat{\mathbf{u}}$ at the boundaries provided that $\partial p/\partial \mathbf{n} = 0$ at the first time step. Despite the fact that this is an approximation to the boundary condition implied by (4), it provides a consistent scheme when used with the homogeneous pressure boundary conditions.[2, 10] Our previous numerical experiments on cavity flows[2] as well as the analysis of Gresho[10] conclusively demonstrate that specifying a slip velocity on the boundaries from (4) for the intermediate velocities gives virtually the same result as using $\hat{\mathbf{u}} = \mathbf{u}^{n+1}$ at the boundaries.
3. Update $\mathbf{u}^{n+1}$ using the relation given by (4):

$$\mathbf{u}^{n+1} = \hat{\mathbf{u}} - \frac{\Delta t}{2}(\nabla p^{n+1} - \nabla p^n). \tag{8}$$

Note that here we are solving for the computational pressure, which is a second-order aproximation to the true pressure (P. M. Gresho, private communication, 1991). A comparison between the present formulation and the original formulation of Kim and Moin,[11] who disregard the pressure term in (3), was done for the unsteady (Re = 30 000) solution and shows that in the latter the velocity amplitudes are approximately 1% smaller than in the former (Figure 2). This result was found to be independent of the time step provided that the Courant number was less than 0·5, which is the limit of stability for both methods. Since by including the pressure the solution procedure becomes fully second-order, we performed the unsteady calculations with this method. However, the solution procedure with the pressure requires storage of one additional array, so that the original method can be preferable if storage is a limiting factor.

With this procedure the Navier–Stokes equations are reduced to a set of Helmholtz equations with Dirichlet/Neumann boundary conditions for the velocities (equation (6)) and a Poisson equation with Neumann boundary conditions for the pressure (equation (7))

The spatial discretization is done on a stretched and staggered meshes as shown in Figure 3. The stretching is computed by the formula

$$x_{ci} = \frac{1}{2}\left[1 - \cos\left(\pi \frac{i-1}{M-1}\right)\right], \quad i = 1, 2, \ldots, M. \tag{9}$$

Similarly y_{cj} are computed for $j = 1, 2 \ldots, N$. It is important that each pressure node is in a cell centre to ensure that continuity is satisfied in the cell. The Neumann boundary conditions for

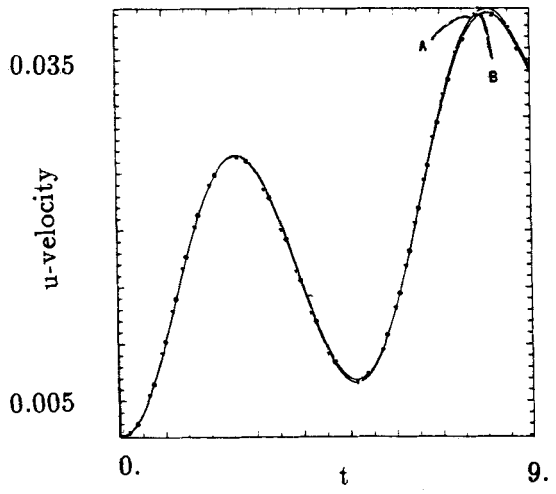

Figure 2. Comparison of velocity signals for two different fractional step formulations ($Re = 30\,000$): A, adding ∇p^n (as in equation (6)); B, neglecting ∇p^n in equation (6)

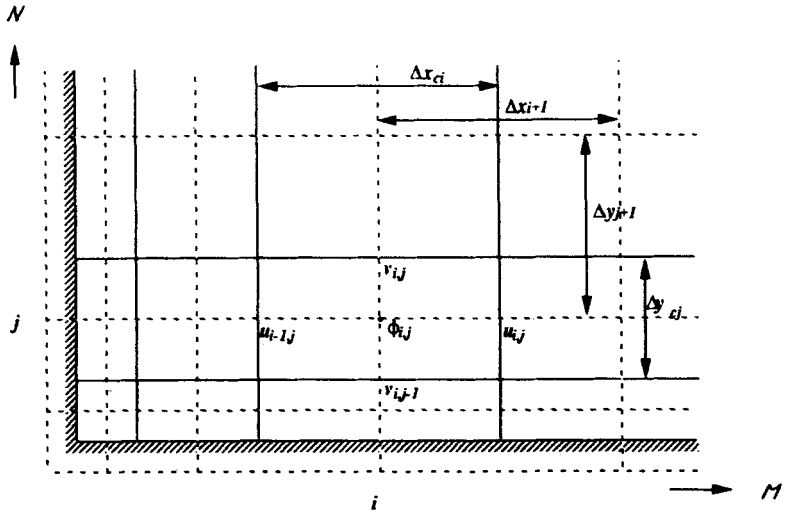

Figure 3. Grid configuration for stretched and staggered mesh:——, grid for velocity nodes; – – –, grid for pressure nodes

pressure are satisfied by placing one pressure node on each side of the boundary, satisfying continuity at the boundaries. Because of the Neumann boundary conditions, after discretization the pressure equation yields a non-positive definite matrix which is singular with one zero eigenvalue. This singularity is avoided by setting the pressure value at one of the boundary points equal to zero. However, the coefficient matrix for pressure is still ill-conditioned and because of the stretched mesh the matrix is also asymmetric. For the solution of this matrix, given the simple geometry, we have found the tensor product method to be highly efficient. This method is briefly described below.

3.1. The tensor product method

The problem under consideration is a Poisson equation on a rectangular domain with full Neumann boundary conditions. This equation can be written as

$$\nabla^2\phi = RHS, \tag{10}$$

where RHS is the source term. The Laplace operator is discretized with second-order finite differences on a five-point stencil. The resulting difference equation reads

$$\phi_{i-1,j}a_i^- - \phi_{i,j}a_i + \phi_{i+1,j}a_i^+ + \phi_{i,j-1}b_j^- - \phi_{i,j}b_j + \phi_{i,j+1}b_j^+ = RHS_{i,j}, \tag{11}$$

where the parameters a and b are defined as (see Figure 2)

$$a_i^- = \frac{1}{\Delta x_i \Delta x_{ci}}, \qquad a_i^+ = \frac{1}{\Delta x_{i+1}\Delta x_{ci}}, \qquad a_i = a_i^- + a_i^+,$$

$$b_j^- = \frac{1}{\Delta y_j \Delta y_{cj}}, \qquad b_j^+ = \frac{1}{\Delta y_{j+1}\Delta y_{cj}}, \qquad b_j = b_j^- + b_j^+.$$

Equation (11) can be written as a matrix product equaton given as

$$\mathbf{A\Phi} + (\mathbf{B\Phi}^{\mathrm{T}})^{\mathrm{T}} = \mathbf{RHS}, \tag{12}$$

where $\mathbf{A}$ is the tridiagonal matrix representing the x-direction finite difference operator,

$$\mathbf{A} = \begin{pmatrix} a_1^- - a_1 & a_1^+ & 0 & 0 & \cdots & 0 \\ a_2^- & -a_2 & a_2^+ & 0 & \cdots & 0 \\ \vdots & \ddots & \ddots & \ddots & & \vdots \\ \vdots & & & & & \vdots \\ 0 & \cdots & 0 & a_{M-1}^- & -a_{M-1} & a_{M-1}^+ \\ 0 & \cdots & 0 & 0 & a_M^- & a_M^+ - a_M \end{pmatrix},$$

$\mathbf{B}$ is similarly a tridiagonal N-dimensional matrix representing the y-direction finite difference operator, $\mathbf{\Phi}$ is the unknown $N \times M$ matrix and $\mathbf{RHS}$ is an $N \times M$ matrix. Note that $\mathbf{\Phi}$ and $\mathbf{RHS}$ are kept in matrix form and not as vectors. This is possible since the operators $\mathbf{A}$ and $\mathbf{B}$ are independent of the y- and x-direction respectively. Using the relation $(\mathbf{B\Phi}^{\mathrm{T}})^{\mathrm{T}} = \mathbf{\Phi B}^{\mathrm{T}}$, equation (12) becomes

$$\mathbf{A\Phi} + \mathbf{\Phi B}^{\mathrm{T}} = \mathbf{RHS}. \tag{13}$$

Then $\mathbf{B}^{\mathrm{T}}$ is decomposed into $\mathbf{B}^{\mathrm{T}} = \mathbf{Q\Lambda Q}^{-1}$ and with this substitution equation (13) can be written as $\mathbf{A\Phi} + \mathbf{\Phi Q\Lambda Q}^{-1} = \mathbf{RHS}$, which becomes

$$\mathbf{A\Phi Q} + \mathbf{\Phi Q\Lambda} = \mathbf{RHSQ}. \tag{14}$$

The matrix product $\mathbf{\Phi Q}$ represents an intermediate unknown matrix $\mathbf{\Psi} = \mathbf{\Phi Q}$. Equation (14) represents N independent sets of tridiagonal linear equations corresponding to one equation for each eigenvalue. This matrix equation (14) can now be solved in three steps.

1. Matrix multiplication: $\mathbf{R} = \mathbf{RHSQ}$.
2. Solve for $\mathbf{\Psi}$: $\mathbf{A\Psi} + \mathbf{\Psi\Lambda} = \mathbf{R}$.
3. Matrix multiplication: $\mathbf{\Phi} = \mathbf{\Psi Q}^{-1}$.

During the second step the tridiagonal matrix is solved N times using the Thomas algorithm. Since in this step only a back substitution is performed for each tridiagonal solver (the LU decomposition is done only at the first time step and is stored for subsequent use), this becomes an efficient algorithm. This step is also vectorized by running the inner loops along the decomposed direction (y-direction). The bulk of the computer work is done in steps 1 and 3 and here we can apply standard high-speed matrix multiplications. The storage requirement for the tensor product method is of order N^2.

For a large number of grid points a direct solution of (11) by Gaussian elimination is not preferable because of the storage requirements. When the matrix is factorized, fill-in occurs between the bands and the storage needed is of order N^4. Owing to rounding errors, solutions of large matrices by Gaussian elimination may also be inaccurate.

For the momentum equations we used both a general purpose conjugate gradient program (ICGC) written by Kapitza and Eppel[12] and the tensor product method described above. ICGC reads the diagonals in a banded matrix and iterations are performed until convergence is reached. For the highly ill-conditioned pressure equation convergence was not reached for large N using this technique. Note that the velocity equations were discretized in the same way as the pressure equation, i.e. using central differences. However, because these are Helmholtz-type equations with Dirichlet boundary conditions, the finite difference matrix is well-conditioned and can be efficiently solved by the conjugate gradient method.

In comparing the tensor product method and ICGC, we found that the fully vectorized tensor product method is more efficient on the Cray Y-MP. The tensor product method is also more applicable and general since there is no need to find an optimal convergence criterion and, owing to machine round-off, it can solve singular matrices.[13] Since we did not try to optimize the IGCG programme, a fair comparison of CPU time use cannot be done and the CPU times reported here are only for the tensor product method.

In all the computations the Courant number was kept below 0·5 to ensure the stability of the solution; here we define the Courant number as $C = \max_{i,j}[(|u_{i,j}|/\Delta x_i + |v_{i,j}|/\Delta y_j)\Delta t]$.

4. RESULTS AND DISCUSSION

In this section we first discuss several cases providing a direct comparison with the results of Ghia *et al.*[1] and Kumagai[3] and also present a mesh refinement study. Subsequently, high-Reynolds-number results are discussed emphasizing the onset of the unsteady flow regime.

4.1. Code verification and mesh refinement study

Two lid-driven cavity cases with $Re_L = 1000$ and 5000 ($Re_L = lu_L/\nu$, where u_L is the lid velocity) were compared with Ghia *et al.*[1] for which streamfunction ψ_{min} and vorticity ζ_{VC} values in the centre of the main eddy are listed in Table I. It is shown that, despite the relatively coarse mesh, the present results compare very favourably with the benchmark study.

Two important issues concerning the numerical method used in this work involve the effect of mesh stretching on the solution accuracy and the mesh independence of the results at high-Reynolds numbers. In Table II the values of Re^B and $\Delta\psi$ are listed for $Re = 100$ and 2000 using several mesh configurations for the shear-driven cavity. Here Re^B is the Reynolds number defined by Bye[4] in terms of the surface velocity (u_s) at the midpoint of the cavity, i.e.

$$Re^B = \frac{u_s}{u_*} Re \tag{15}$$

(Re^B can be directly compared with Re_L) and $\Delta\psi$ is defined as $\Delta\psi = \psi_{max} - \psi_{min}$.

Table I. Comparison between results of Ghia *et al.*[1] and present calculations for lid-driven cavity for two Reynolds numbers

$Re=1000$	ψ_{min}	ζ_{VC}	$Re_L=5000$	ψ_{min}	ζ_{VC}
Present, 81×81 stretched	−0·1175	−2·035	Present 81×81 stretched	−0·1219	−2·001
Ghia *et al.*, 129×129 constant	−0·1197	−2·050	Ghia *et al.*, 257×257 constant	−0·1190	−1·8602

Table II. Effect of mesh resolution on steady state results for low Reynolds numbers and comparison with Kumagai's results[3]

$Re=100$	Re^B	$\Delta\psi$	$Re=2000$	Re^B	$\Delta\psi$
81×81 stretched	1·685	$1{\cdot}561\times10^{-3}$	55×55 stretched	291·20	$1{\cdot}625\times10^{-2}$
41×41 stretched	1·681	$1{\cdot}569\times10^{-3}$	41×41 stretched	288·45	$1{\cdot}634\times10^{-2}$
33×33 stretched	1·688	$1{\cdot}593\times10^{-3}$	33×33 stretched	285·90	$1{\cdot}636\times10^{-2}$
81×81 constant	1·687	$1{\cdot}551\times10^{-3}$	55×55 constant	298·60	$1{\cdot}5804\times10^{-2}$
41×41 constant	1·694	$1{\cdot}564\times10^{-3}$	41×41 constant	300·3	$1{\cdot}572\times10^{-2}$
41×41 constant[3]	1·735	$1{\cdot}55\times10^{-3}$	41×41 constant[3]	300·0	$1{\cdot}55\times10^{-2}$
			33×33 constant	303·2	$1{\cdot}567\times10^{-2}$

Accordingly, the results obtained with both the stretched and constant mesh configurations are consistent, i.e. with increasing mesh resolution, Re^B and $\Delta\psi$ converge to a constant value. These tabulated values also indicate good quantitative agreement with Kumagai's[3] results for which the $\Delta\psi$ were determined from the streamfunction plots and are accurate only up to two digits.

A mesh resolution study was also conducted for the $Re=30\,000$ case during the final stages of the calculations on an 81×81 grid and on a 161×161 grid for a short time period (Figures 4 and 5 respectively). Streamfunction contours at four different times 0·50 time units apart display a high similarity between the high- and low-mesh calculations, with a more detailed contour map for the fine mesh results. Furthermore, in Table III almost no difference is observed between the values of Re^B and $\Delta\psi$ calculated for these two cases. Therefore it can be asserted that the 81×81 grid provides adequate resolution.

On the basis of this mesh resolution study it can be concluded that the use of a stretched mesh does not degrade the solution accuracy and gives satisfactory results. It is also clear that a stretched mesh is preferable at high Reynolds numbers where the velocity gradients are large close to the boundaries; a fine mesh in these regions will ensure proper resolution of these gradients. We have also been able to determine the mesh resolution that provides the desired accuracy at high Reynolds numbers and is still feasible for very-long-term computations involving several hundred thousand time steps (Table IV) required for convergence for high-Reynolds-number oscillatory solutions.

4.2. Low-Reynolds-number cases

Two cases with $Re=100$ and 2000 were considered and the ensuing steady state solutions compared with Kumagai's[3] results which he obtained by numerically integrating the steady state

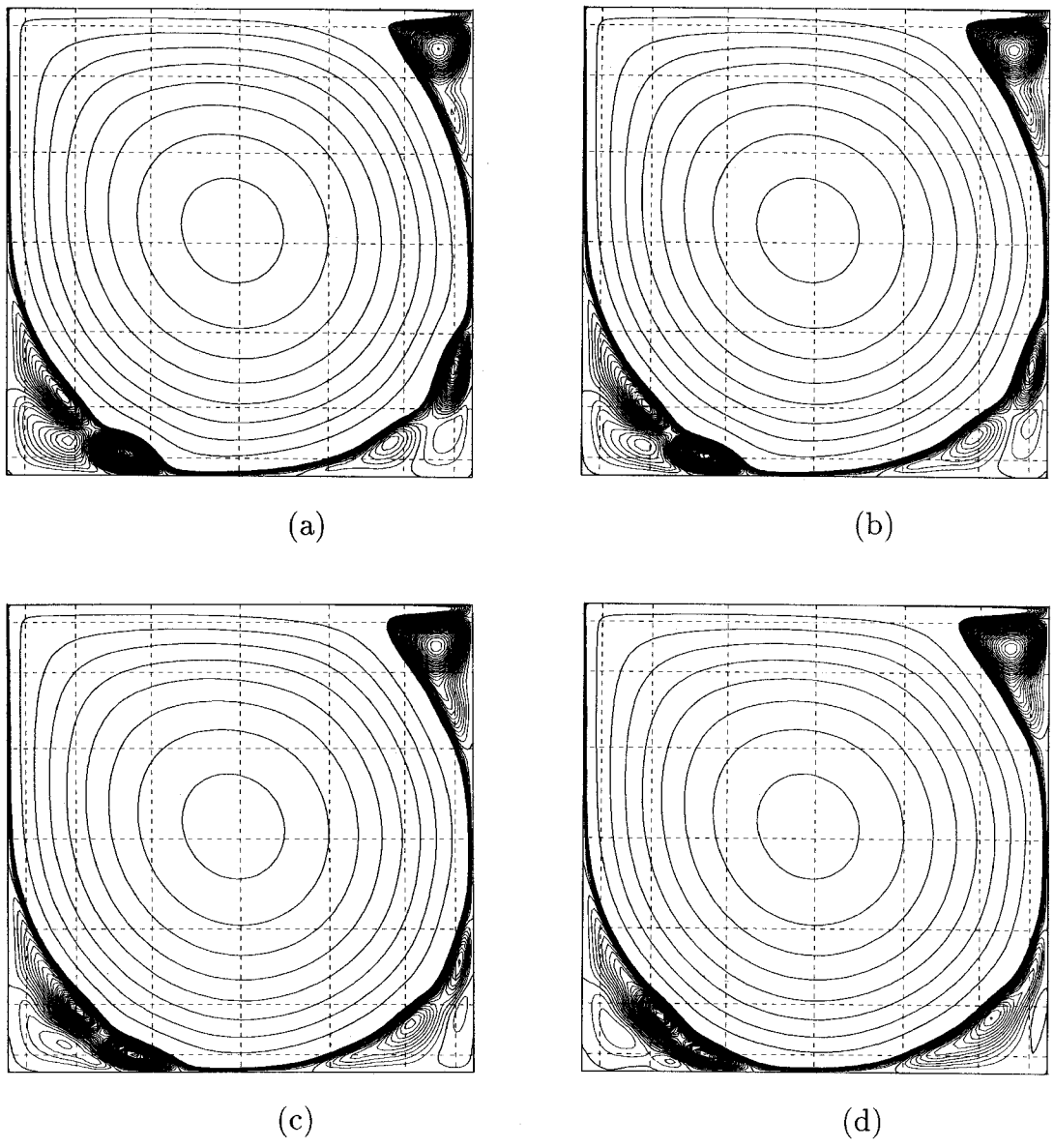

Figure 4. Steamfunction contours for $Re = 30\,000$ on 81×81 grid: (a) $t = 5000{\cdot}5$; (b) $t = 5001{\cdot}0$; (c) $t = 5001{\cdot}5$; (d) $t = 5002{\cdot}0$ (increment 0·005 for main eddy and $5{\cdot}0 \times 10^{-5}$ in corners; every 10th grid line shown dahsed)

governing equations in vorticity–streamfunction form by an alternating direction (ADI) implicit scheme. For $Re = 100$ the streamfunction and vorticity contours obtained from the present calculations (Figures 6(a) and 6(b), respectively) display a main centre vortex and one large secondary vortex at each lower corner of the cavity; the solution is symmetric around the central axis. For $Re = 2000$ the steady state results (Figures 7(a) and 7(b)) indicate movement of the main vortex centre to the left and enlargement of the left corner eddy. The formation of secondary corner vortices is also apparent from the streamfunction contours (Figure 7(a)). Comparison with

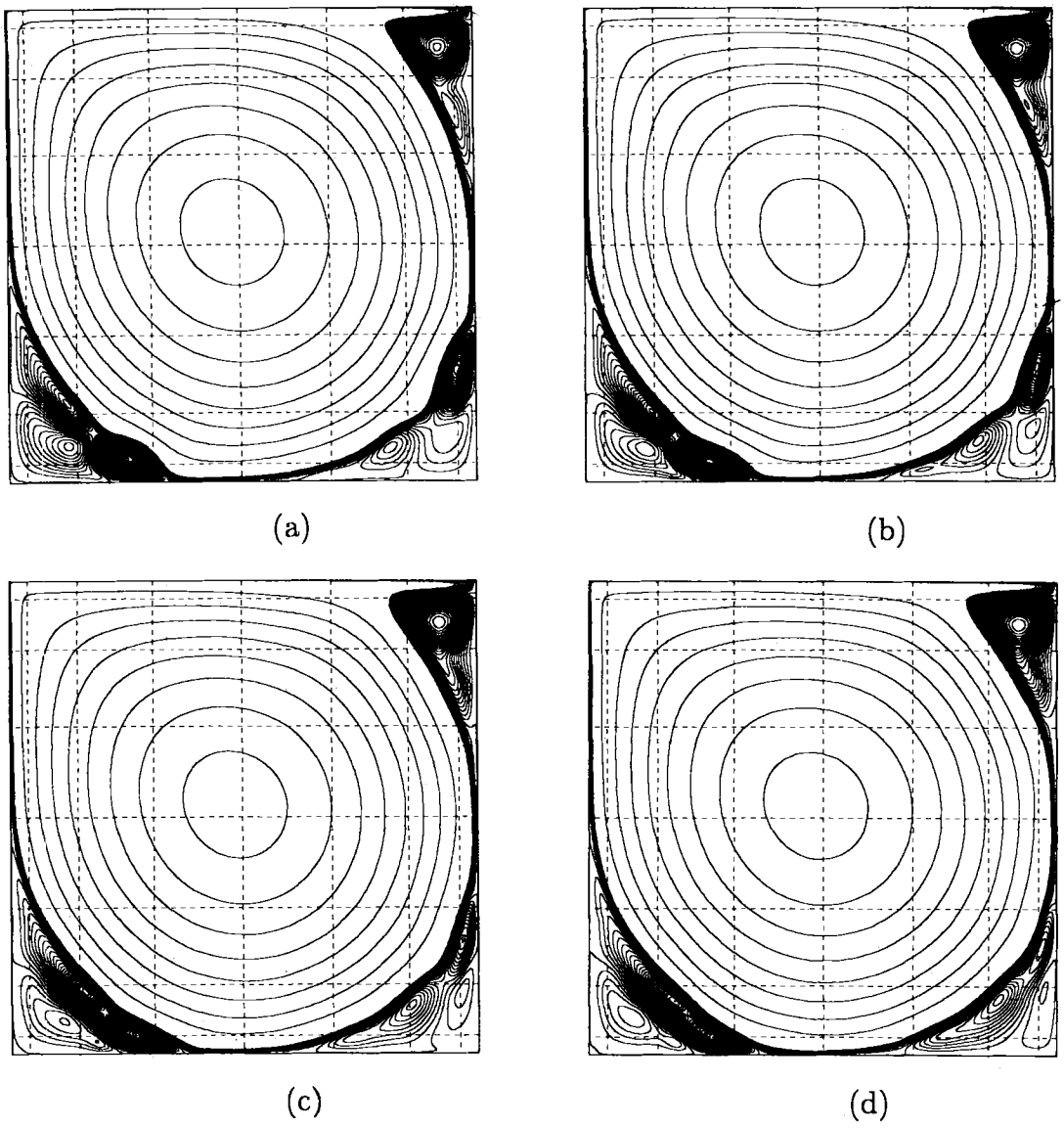

Figure 5. Streamfunction contours for $Re = 30\,000$ on 161×161 grid: (a) $t = 5000{\cdot}5$; (b) $t = 5001{\cdot}0$; (c) $t = 5001{\cdot}5$; (d) $t = 5002{\cdot}0$ (increment 0·005 for main eddy and $5{\cdot}0 \times 10^{-5}$ in corners; Every 20th grid line shown dashed)

Table III. Results of final stages for $Re = 30\,000$ with different mesh resolutions

	$t = 5001$		$t = 5002$		
Grid	Re^B	$\Delta\psi$	Re^B	$\Delta\psi$	CPU seconds per time step
81×81	11006·4	0·04724	11217·6	0·0463	0·033
161×161	10993·2	0·04617	11201·1	0·0450	0·194

Table IV. Results of high-Reynolds-number calculations

	$Re = 10000$	$Re = 30000$
Re^B	2593	11100*
$\Delta\psi$	0·0327	0·04*
Δt	0·009	0·005
t_{fin}	400	5000
Grid	61×61	81×81

* Averaged values.

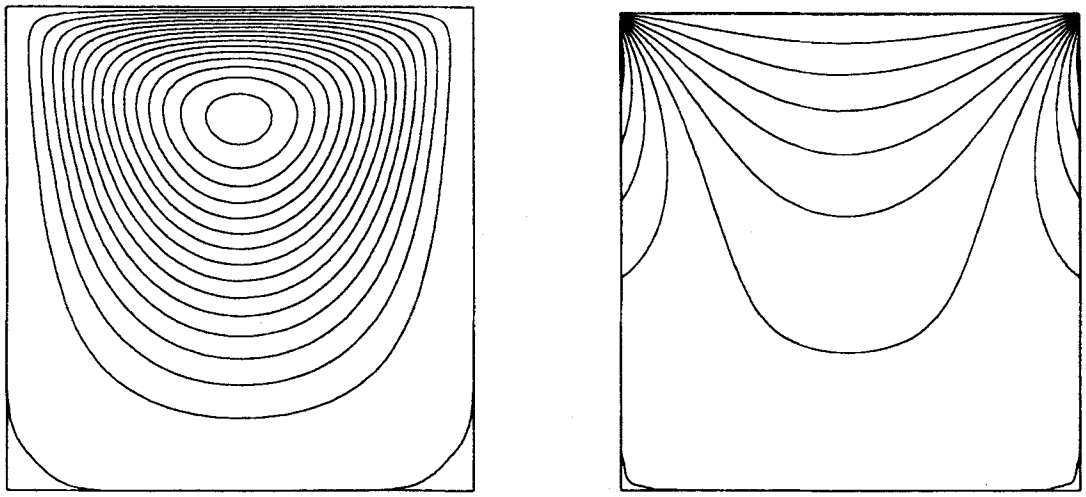

Figure 6. Steady state solution for $Re = 100$: (a) streamfunction contours (increment 0·0001); (b) vorticity contours (increment 0·02)

the results of Kumagai[3] reveals a strong similarity. As a notable exception to this similarity, Kumagai's results indicate that the high vorticity gradients forming at the upper (singular) corners for $Re = 100$ elongate and move away from the upper boundary with increasing Reynolds number (Figure 2(a) of his paper). This phenomenon is not physical but is purely an artifice ensuing from the selection of maximum/minimum contour levels to be plotted. As expected, if the calculated maximum level is included, the high-vorticity-gradient region always remains at the interface (Figure 7(b)).

4.3. High-Reynolds-number effects

In shear-driven cavity flows the Reynolds number is proportional to the driving shear directly influencing the flow dynamics. When the Reynolds number increases, effects of viscosity are confined to a thin layer close to the solid boundaries, including high gradients in the shear stress distribution. The local curvature of the resulting mean velocity profiles (Figures 8(a)–8(e)) also increases. As evident from the reverse flow indicated in these figures, small eddies develop in the

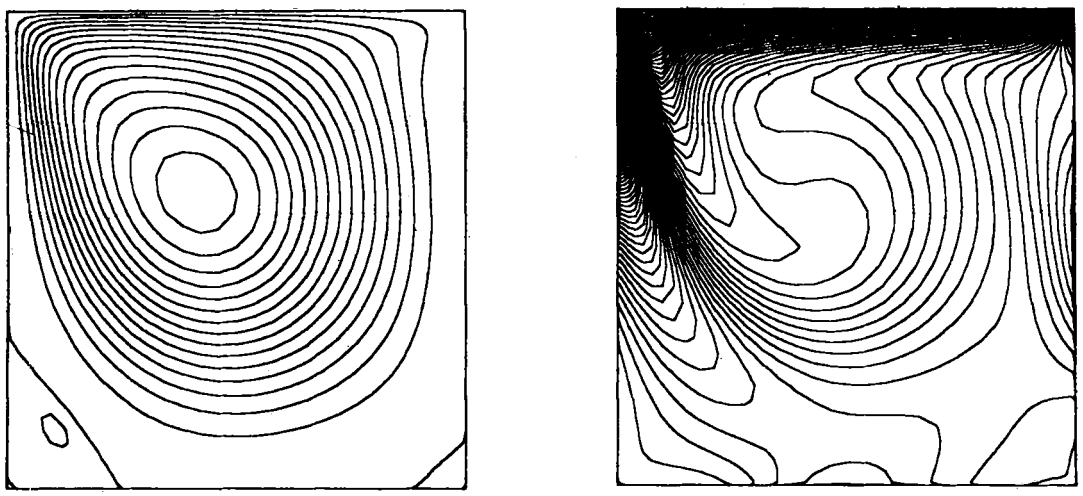

Figure 7. Steady state soluton for $Re = 2000$: (a) streamfunction contours (increment 0·001 in centre and $5{\cdot}0 \times 10^{-6}$ in corners); (b) vorticity contours (increment 0·02)

vicinity of the two lower corners (and also at the upper right corner) and the laminar mean velocity becomes unstable. The interaction of these eddying motions with the mean shear eventually leads to turbulence. Because of the two-dimensionality of the mathematical model, the present simulations will be limited to the unsteady (unstable) flow regime prior to the onset of turbulence.

The high-Reynolds-number calculations were done for $Re = 10\,000$ and 30 000. Note that according to Keulegan's experimental results,[14] in the wind-driven cavity, transition from laminar to turbulent flow may occur for Re^B between 400 and 1000. Similarly, on the basis of an analysis using the steady state Navier–Stokes equations, Bye[4] determined a range of transition Re^B between 400 and 600. Furthermore, Kumagai[3] roughly estimated transition to occur at even lower Re^B, although he strongly cautioned aganst the accuracy of such data obtained from the steady state equations. Both authors used the formation of an inflectional velocity profile indicating reverse flow as the criterion for the onset of the unsteady regime.

In the present work the convergence of the solutions was measured in terms of the total kinetic energy, the time history of which is displayed in Figure 9(a) for $Re = 10\,000$. As evident from this figure, the solution converges to a steady state at about $t = 400$ and the absence of any oscillations indicates steady flow. The calculated value of Re^B in this case is $Re^B = 2593$, which is much higher than the transition values obtained by Kumagai[3] and Bye[4] and lends strong evidence to the inadequacy of their steady state model to predict the onset of transition. It is interesting to note that in Figure 8 the velocity profiles for $Re = 2000$ and 10 000 (equivalent to $Re^B = 291{\cdot}2$ and 2593 respectively) do display regions of strong reverse flow. However, the solutions converge to a steady flow regime, refuting the use of the 'inflectional velocity profile' criterion for the bifurcation to an unsteady state in the absence of side wall effects. The experiments of Keulegan[14] were likely influenced by the finite spanwise aspect ratio to undergo transition at a much lower Re^B than in the case of the computation at infinite aspect ratio.

The steady state streamfunction and vorticity contours are presented in Figures 9(b) and 9(c) respectively for the $Re = 10\,000$ case. Comparison of the vorticity contours with the correspond-

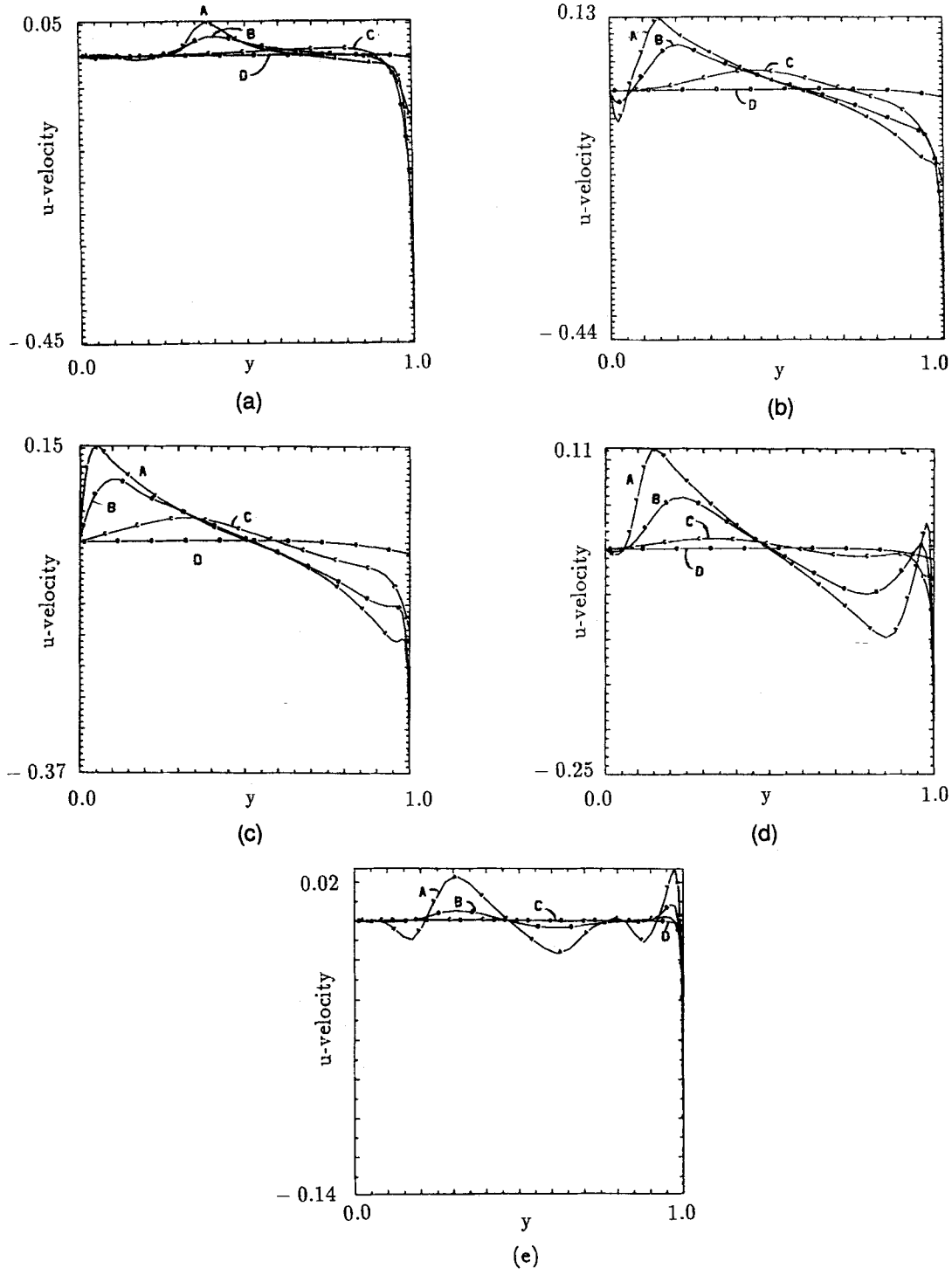

Figure 8. Horizontal velocity (u) profiles in cavity at (a) $x=0{\cdot}037$, (b) $x=0{\cdot}24$, (c) $x=0{\cdot}5$, (d) $x=0{\cdot}76$ and (e) $x=0{\cdot}96$: A, $Re=30\,000$; B, $Re=10\,000$; C, $Re=2000$; D, $Re=100$

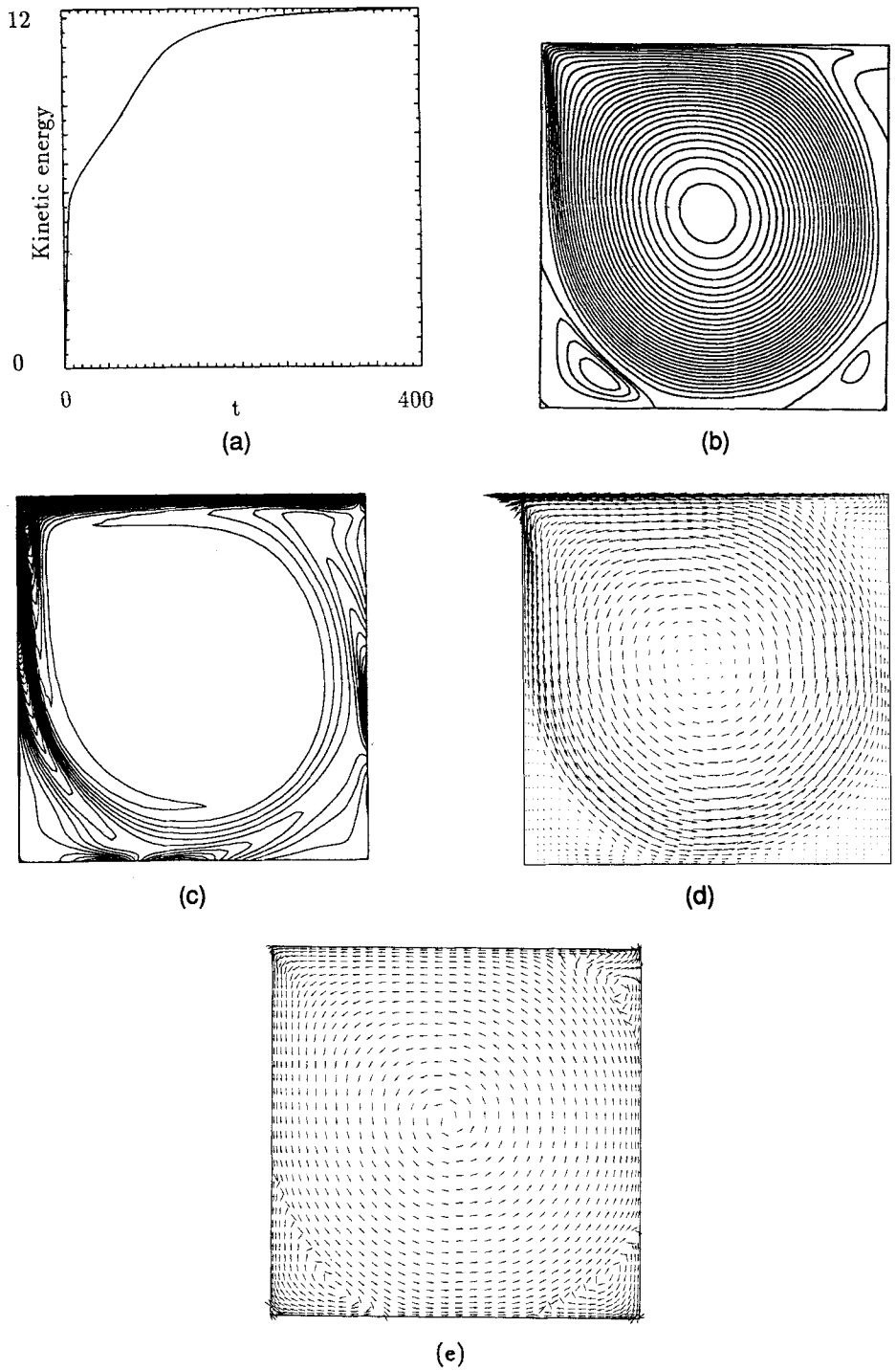

Figure 9. Steady state results for $Re = 10\,000$: (a) time history of total kinetic energy; (b) streamfunction contours (increment 0·001 in centre and 0·0002 in corners); (c) vorticity contours (increment 0·3); (d) velocity vectors with vector length proportional to velocity magnitude; (e) constant length velocity vectors

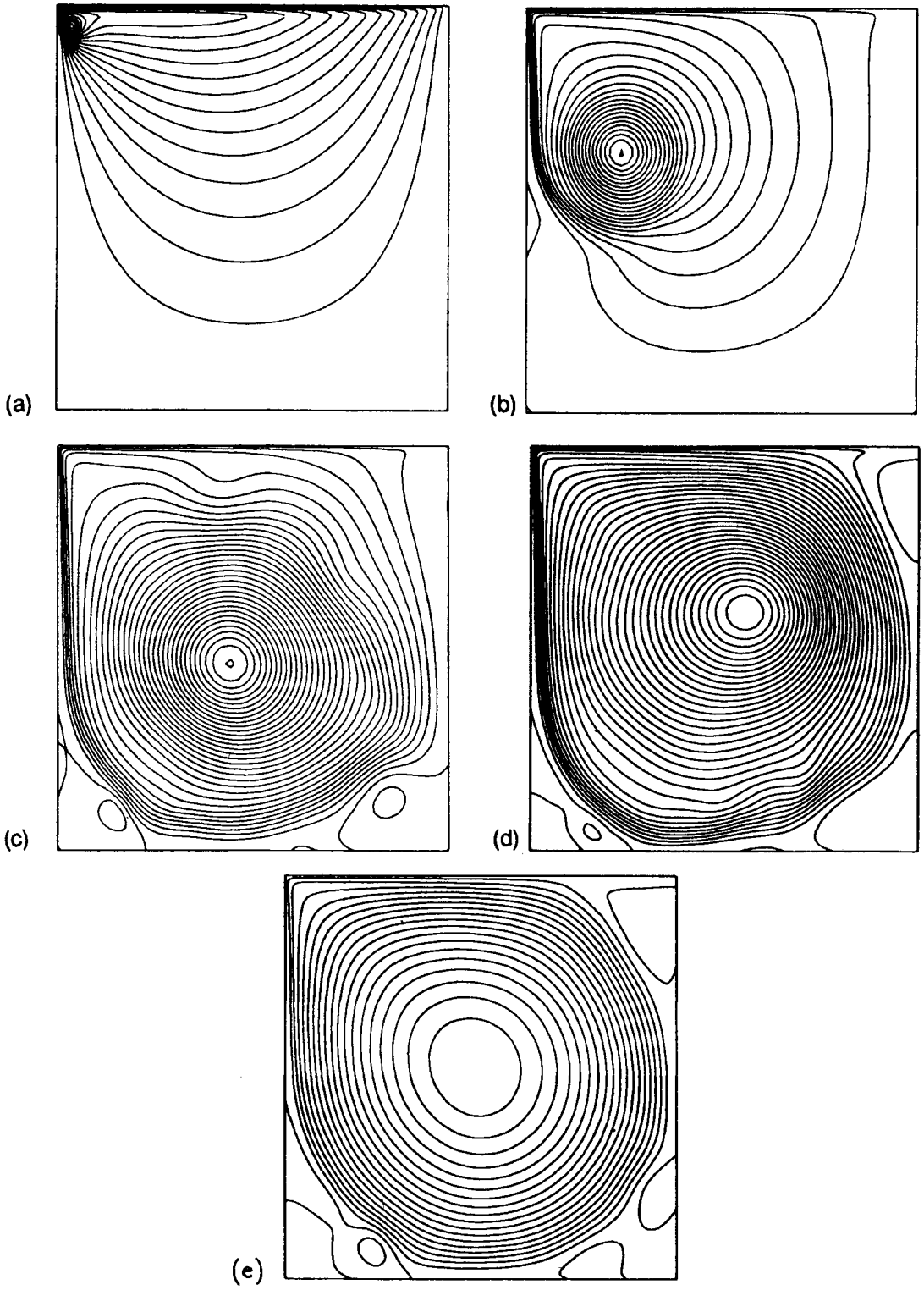

Figure 10. Streamfunction contours for $Re = 30\,000$ on 81×81 grid: (a) $t = 2{\cdot}5$; (b) $t = 20$; (c) $t = 60$; (d) $t = 90$; (e) $t = 870$ (increment 0·001 for (a)–(d) and 0·002 for (e))

ing results at $Re = 100$ and 2000 (Figures 3(b) and 4(b) respectively) reveals that the high-velocity-gradient regions move towards the boundaries as the Reynolds number increases. The steamfunction contours manifest essentially the same flow patterns for all three cases (Figures 6(a), 7(a) and 9(b)), characterized by one primary eddy occupying the centre of the cavity and one

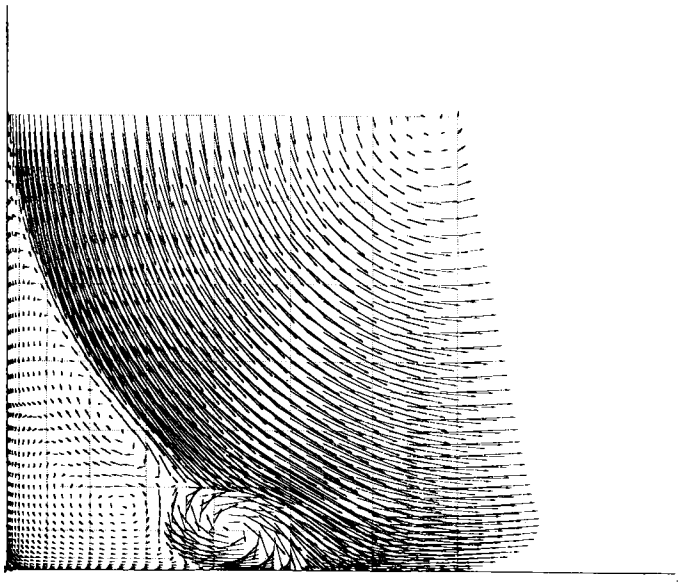

(a)

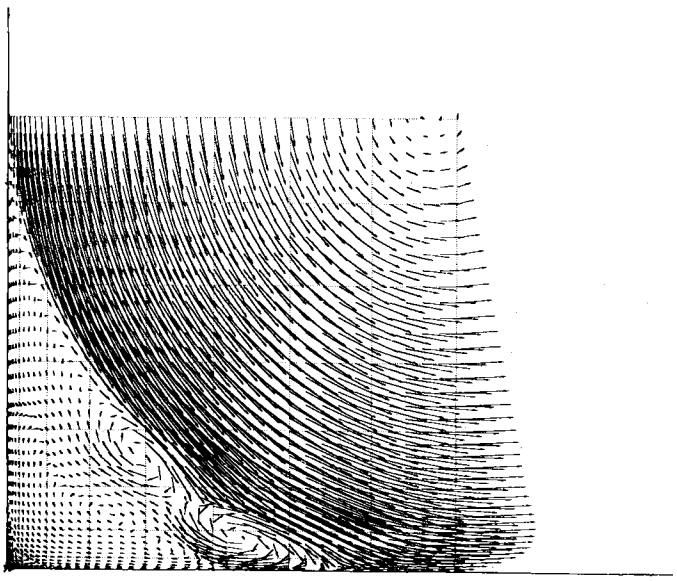

(b)

Figure 11. Velocity vectors showing evolution of flow in lower left corner with vector length proportional to velocity magnitude. Snapshots taken at 0·25 time unit intervals starting at $t = 5000$

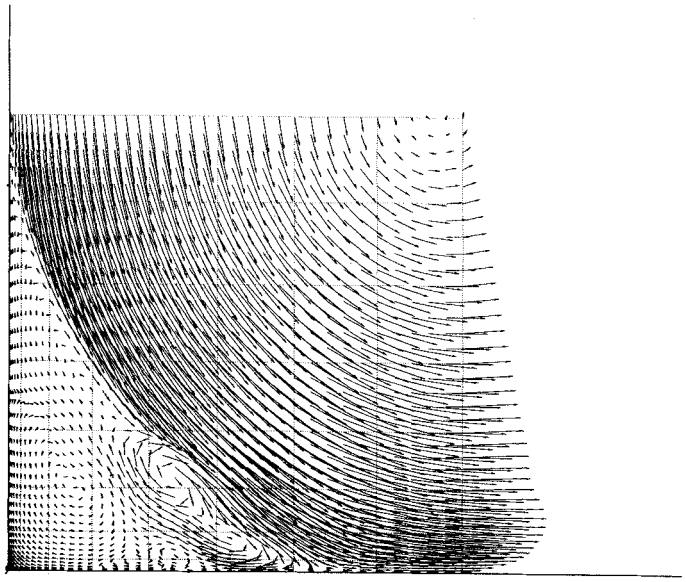

(c)

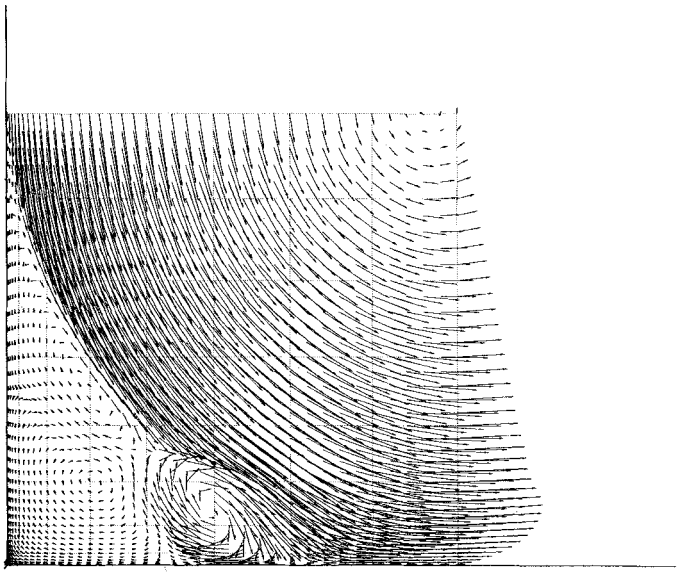

(d)

Figure 11. (Continued)

secondary eddy at each of the three corners; tertiary eddies develop at the lower corners as the Reynolds number increases. Figures 9(d) and 9(e) contain velocity vectors highlighting the details of the vortical flow in the cavity.

In Figures 10(a)–10(e) streamfunction contours plotted at several instants in time display the flow evolution for $Re = 30\,000$, including the start-up period. As the flow develops, the flow field

becomes more complex and several vortices form at each corner of the cavity, except the upper downstream corner. These small eddies are unstable and oscillatory and their strength also varies with time. The details of this vortical activity are documented in Figures 11(a)–11(d), in which enlarged snapshots of velocity vectors in the vicinity of the lower left corner are presented at 0·25 time unit intervals starting with $t = 5000$. These eddies are driven by the high velocity imparted from the main vortex and are associated with high root-mean-square (RMS) intensities of the velocity fluctations (see Figures 14(a)–14(c)). The eddies in the lower right corner are also unstable, but they have less momentum and therefore oscillate with less strength. The oscillatory motion energized in the corners in turn influences the flow in the cavity centre and induces oscillations on the main vortex. Similarly to the $Re = 10\,000$ case the time evolution of the total kinetic energy in the cavity was plotted to follow the convergence of the solution to a statistically steady state. This is documented in Figure 12(a) and displays the approach of the kinetic energy to a constant mean value at about $t = 2000$. The constant mean value indicates a balance between energy production and dissipation in the cavity, while the oscillatory behaviour about the mean implies an unsteady motion. Consequently, it is apparent that for this Reynolds number, for which we calculate $Re^B = 11\,100$, the flow becomes unsteady and unstable. This value of Re^B at which the flow becomes unstable is about one order of magnitude higher than those estimated by Kumagai[3] and Bye.[4] Figure 12(b), where the kinetic energy is recorded from $t = 210$ to 285 using two different Δt values ($\Delta t = 0{\cdot}005$ and 0·0025), indicates that the unsteady solution is independent of the step size and that the oscillations appearing in the solution are physical and not numerical.

Another interesting observation is that the recirculation zone in the lower left corner grows with increasing Reynolds number (see Figures 6(a), 7(a) and 9(b)). When transition occurs, the single corner eddy breaks down into several smaller eddies (Figure 11). This is in agreement with Sethian and Ghoniem's[9] calculations for the backward-facing step flow, where the reattachment length increases until transition starts and the unsteady regime is characterized by more than one eddy in the wake behind the step. The existence of small eddies downstream of the corner eddy at high Reynolds numbers is a result of decreasing diffusive length scale with increasing Reynolds numbers. At low Reynolds numbers the diffusive length scale is large so that small scales of motion (small eddies) are rapidly dissipated by the action of viscosity.

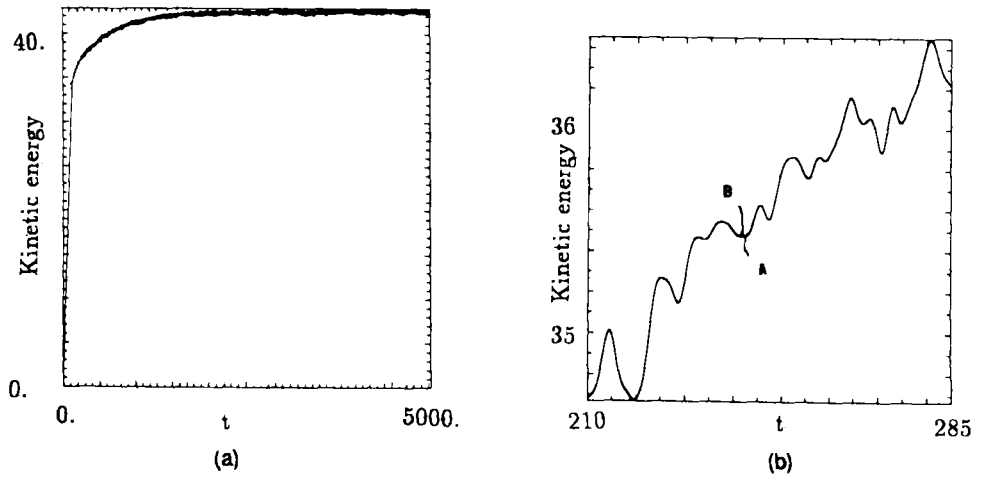

Figure 12. Time history of total kinetic energy for $Re = 30\,000$ (a) from $t = 0$ to 5000 and (b) from $t = 210$ to 285: A, $\Delta t = 0{\cdot}005$; B, $\Delta t = 0{\cdot}0025$

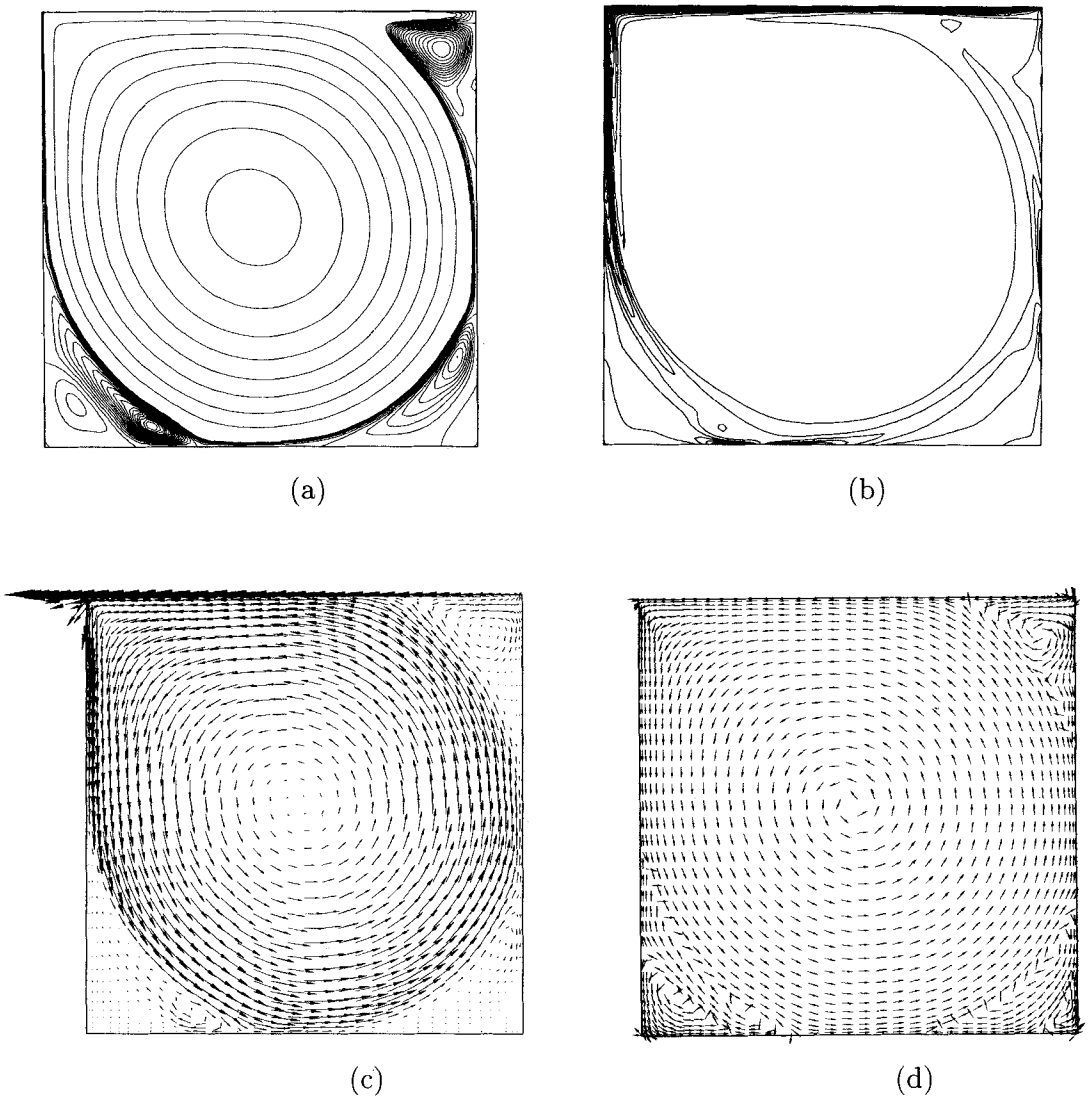

Figure 13. Time-averaged flow field quantities for $Re = 30\,000$: (a) streamfuncton contours (increment 0·005 in centre and $0{\cdot}5 \times 10^{-5}$ in corners); (b) vorticity contours (increment 2·0); (c) velocity vectors with vector length proportional to velocity magnitude; (d) constant length velocity vectors

The mean velocity and the RMS values of the fluctations were obtained by averaging the velocity field from $t = 5000$ to 5100. Figure 13(a) furnishes the time-averaged streamfunction contours exposing the multivortex structures at the three corners of the cavity. The time-averaged vorticity contours (Figure 13(b)) indicate the concentration of the mean vorticity in a very thin region along the upper and left boundaries. Mean velocity vectors are displayed in Figures 13(c) and 13(d) indicating the mean circulatory motion in the cavity. In both lower corners of the cavity multivortex structures are observed. The RMS values of the fluctating velocities and the shear stress, i.e. the non-zero components of the Reynolds stress tensor, were also calculated. The

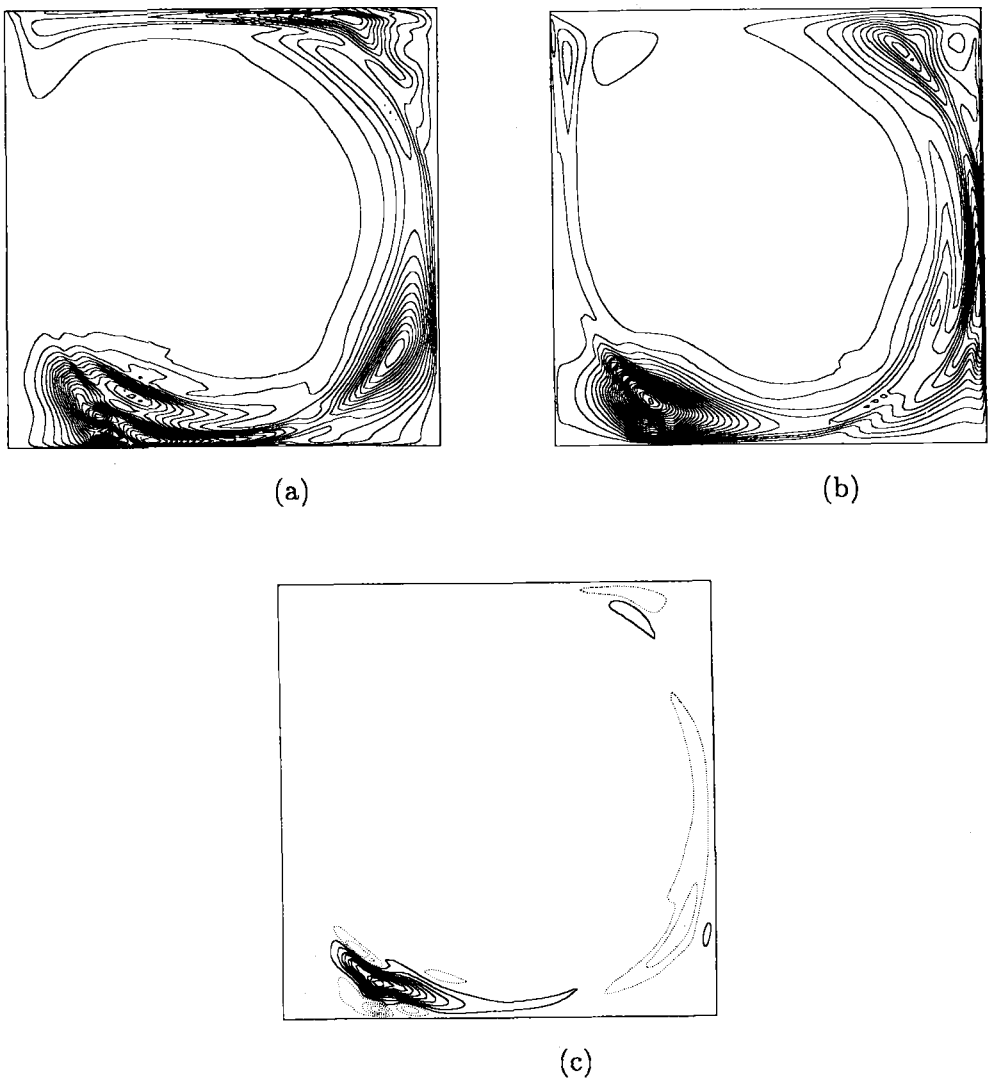

Figure 14. Reynolds stress contours for $Re = 30\,000$: (a) RMS-u (increment 0·001); (b) RMS-v (increment 0·001); (c) shear stress (increment $3{\cdot}2 \times 10^{-5}$); dashed lines indicate negative, solid lines positive contours

contours of these 'turbulent' quantities are concentrated close to the corners and along the bottom and right walls of the cavity (Figures 14(a)–14(c)); the largest magnitudes appear in the regions occupied by the most energetic eddies. The RMS profiles of the fluctating velocity components and the shear stress (Figures 15(a)–15(c)) reveal that the highest RMS u-value obtained is about 2·5%, indicating a substantial intensity of the oscillatory motion, which, as expected, has not reached a turbulent state.

Time variations of the fluctating velocities were recorded at two locations in the vicinity of the left corner where the strongest oscillations take place. For the location corresponding to $x = y = 0{\cdot}037$ (point A), which is interior to the region with high Reynolds stress amplitudes, the time history of the v-velocity (Figure 16(a)) and the u–v phase portrait (Figure 16(b)) were also

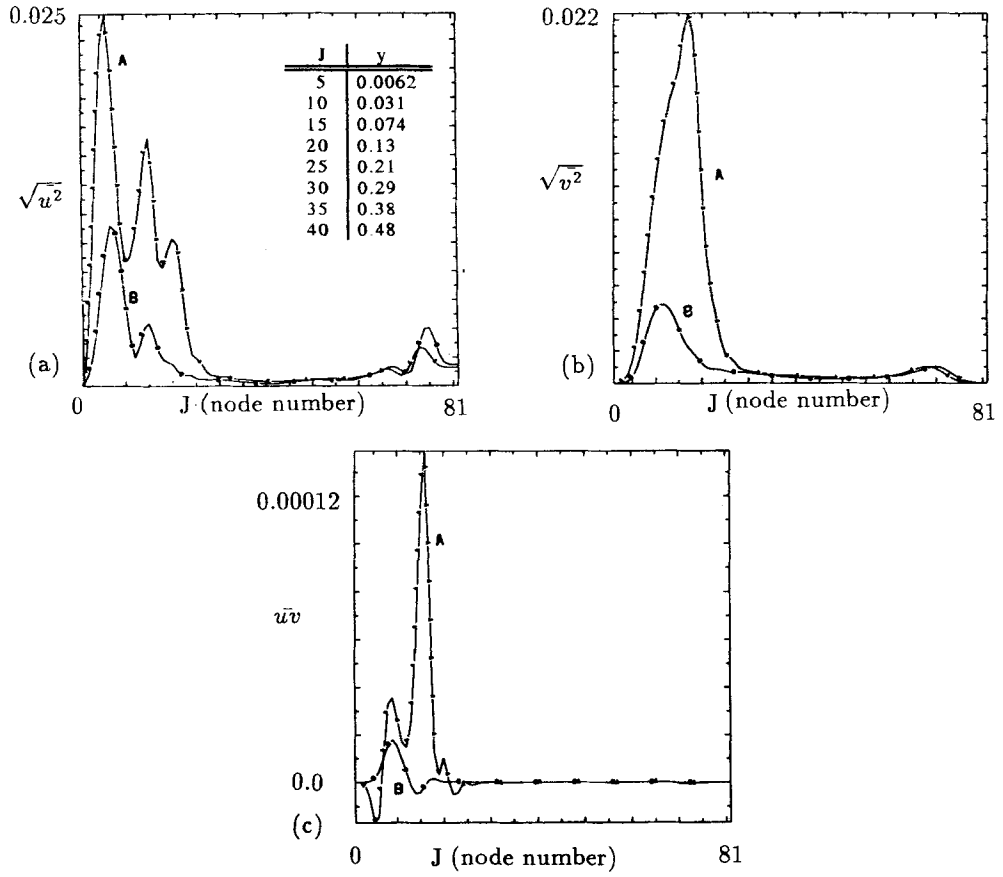

Figure 15. Reynolds stress profiles for $Re = 30\,000$: (a) RMS-u; (b) RMS-v; (c) shear shress; A, $x = 0{\cdot}21$; B, $x = 0{\cdot}5$

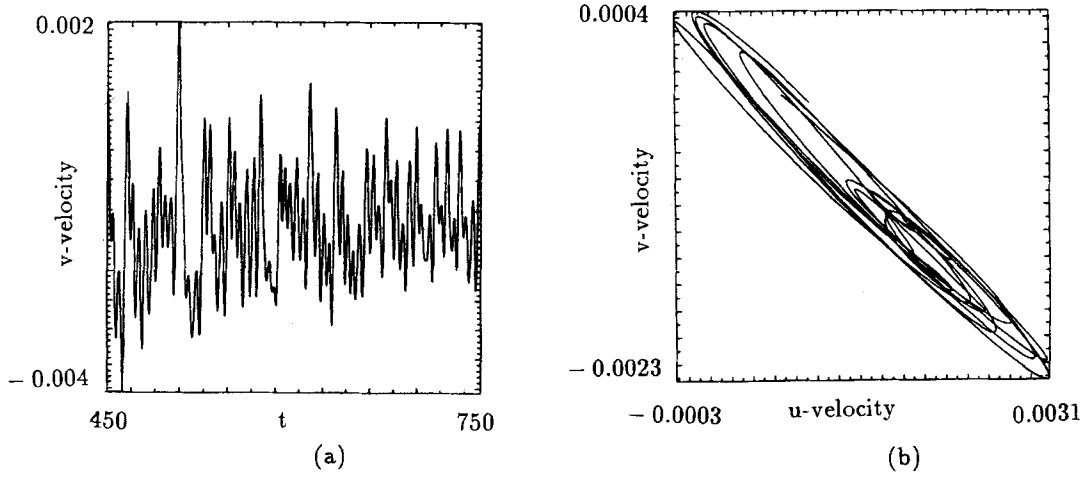

Figure 16. Velocity signal at $x = y = 0{\cdot}037$: (a) v-velocity time history; (b) u-v phase portrait

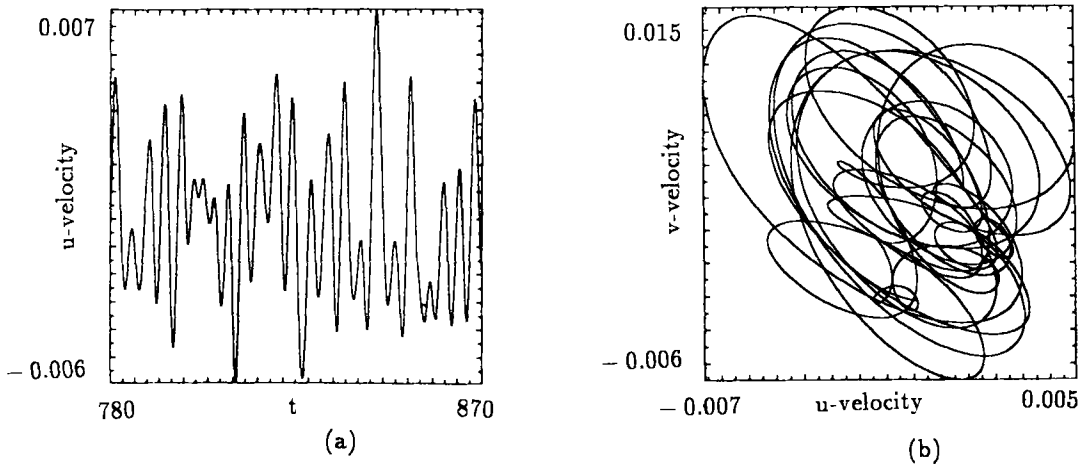

Figure 17. Velocity signal at $x=0{\cdot}20$, $y=0{\cdot}084$: (a) u-velocity time signal; (b) u–v phase portrait

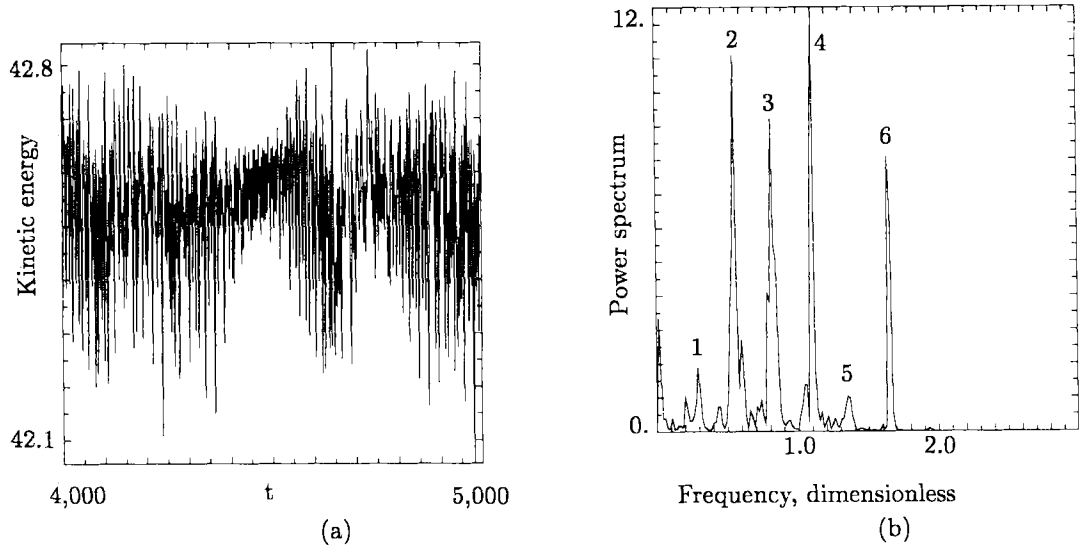

Figure 18. (a) Total kinetic energy from $t=4000$ to 5000. (b) Power spectrum: 1, frequency $f=0{\cdot}28$; 2, $f=0{\cdot}56$; 3, $f=0{\cdot}84$; 4, $f=1{\cdot}12$; 5, $f=1{\cdot}40$; 6, $f=1{\cdot}68$

calculated. The phase portrait (Figure 16(b)) reveals an almost periodic motion which converges upon a loosely banded elliptic orbit. The absence of a tight limit cycle indicates that the flow is unsteady but not rigidly periodic. The u–v phase portrait obtained at point B (corresponding to $x=0{\cdot}20$, $y=0{\cdot}084$) has a spaghetti-like appearance (Figure 17(b)), indicating a greater degree of disorder in comparison with the signal recorded at point A. Note that point A is located close to the corner walls that restrict the oscillatory motion, whereas point B is located in the region with large Reynolds stresses, farther away from the walls. Consequently, oscillations are not restricted and the eddies are free to move with the energy transferred to them from the primary vortex. Finally, the power spectrum for the total kinetic energy signal during the last 1000 time units

(Figure 18(a)) was calculated and shows that frequencies with a multiple of 0·28 clearly have distinct energy peaks, with the most energetic frequency at $4 \times 0{\cdot}28$ (Figure 18(b)). The frequency 0·28 scales to the rotation rate of the main eddy. This rotation rate is approximated from Figure 8(c) by the average slope of curve A between $y = 0{\cdot}1$ and 0·9.

5. CONCLUSIONS

In this work a numerical study was presented to investigate high-Reynolds-number effects in shear-driven cavity flows. The two-dimensional time-dependent Navier–Stokes equations were integrated by a time-splitting technique using second-order finite differences on a staggered and stretched mesh. The Helmholtz equations resulting from the discretization of the momentum equations and the pressure Poisson equation were solved by a tensor product method obviating the use of factorization.

The present simulations using a time-accurate mathematical model provided an estimate of the onset of oscillatory flow (e.g. an estimate of the critical Reynolds number), indicating that the two-dimensional shear-driven cavity flow becomes unsteady and unstable for Reynolds numbers around 30 000, which is about one order of magnitude higher than earlier estimates based on steady state calculations. The present calculations also revealed that the flow is continuously evolving in the unsteady state. After a start-up period, no more energy is accumulated by the flow and a balance is established between the energy imparted to the flow by the driving surface shear and the energy dissipated owing to viscosity.

ACKNOWLEDGEMENTS

This work was sponsored in part by NASA grant NAG-1-798. The first author gratefully acknowledges The Royal Norwegian Council for Scientific and Industrial Research (NTNF) for providing a fellowship.

REFERENCES

1. U. Ghia, K. N. Ghia and C. T. Shin, 'High-*Re* solutions for incompressible flow using the Navier–Stokes equations and a multigrid method', *J. Comput. Phys.*, **48,** 387 (1982).
2. S. Biringen and G. Danabasoglu, 'Oscillatory flow with heat transfer in a square cavity', *Phys. Fluids A*, **1,** 1796–1812 (1989).
3. M Kumagai, 'A numerical study of wind-driven circulation in rectangular cavities', *J. Comput. Phys.*, **47,** 130–145 (1982).
4. J. A. T. Bye, 'Numerical solutions of the steady-state vorticity equation in rectangular basins', *J. Fluid Mech.*, **26,** 577–598 (1966).
5. J. Wu, 'Wind-induced drift currents', *J. Fluid Mech.*, **68,** 49–70 (1975).
6. K. Gustafson and W. Wyss, 'Time-asymptotic flow calculation', *Comput. Phys. Commun.*, **65,** 107–116 (1991).
7. J. R. Koseff and R. L. Street, 'On end wall effects in a lid-driven cavity flow', *J. Fluids Eng.*, **106,** 385–389 (1984).
8. A. K. Prasad and J. R. Koseff, 'Reynolds number and end-wall effects on a lid-driven cavity flow', *Phys. Fluids A*, **2,** 208–218 (1989).
9. J. A. Sethian and A. F. Ghoniem, 'Validation study of vortex methods', *J Comput. Phys.*, **74,** 283–317 (1988)
10. P. M. Gresho, 'On the theory of semi-implicit projection methods for viscous incompressible flow and its implementation via a finite element method that also introduces a nearly consistent mass matrix. Part 1: Theory', *Int. j. numer. methods fluids*, **11,** 587–620 (1990).
11. J. Kim and P. Moin, 'Application of a fractional-step method to incompressible Navier–Stokes equations', *J. Comput. Phys.*, **59,** 308–323 (1985).
12. H. Kapitza and D. Eppel, 'A 3-D Poisson solver based on conjugate gradients compared to standard iterative methods and its performance on vector computers', *J Comput Phys.*, **68,** 474–485 (1978).
13. L. P. Peltier, S. Biringen and A. Chait, 'Application of implicit numerical techniques to the solution of the three-dimensional diffusion equation', *Numer. Heat Transfer*, **18,** 205–219 (1990).
14. G. H. Keulegan, *J Res. NBS*, **46,** 358 (1951).